Time-Resolved Imaging of the Cellular Structure of Methane and Natural Gas Detonations

Mark D. Frederick*[1], Rohan M. Gejji[1], Joseph E. Shepherd[2], and Carson D. Slabaugh[1]

[1]Purdue University, West Lafayette, IN 47907, USA
[2]California Institute of Technology, Pasadena, CA 91125, USA

Abstract We present experimental observations of the density field and reaction structure of methane and natural gas detonation waves propagating in a narrow channel. Simultaneous time-resolved schlieren and CH* chemiluminescence images are used to describe the structure of the unstable front. Nitrogen dilution concentration is varied and effect of increasing dilution is to increase the instability level and cell size and decrease the chemiluminescence intensity. Comparison is made between methane and natural gas fueled detonations. The effect of the higher hydrocarbons present in natural gas, primarily ethane, is to increase the fine-scale structure of the detonation front and create a more continuous reaction front. Utilizing the simultaneous images, observations are made about the formation and dissipation of the material separated across the shear layer behind the front.

Keywords Hydrocarbon detonation · Schlieren · CH* chemiluminescence · Cellular structure · Narrow channel

1 Introduction

Investigation of detonation initiation in methane and natural gas mixtures began in the 1960 and 70s as liquefied natural gas (LNG) became a critical component of the global economy for power generation and heating [1]. The potential for a LNG-air detonation to occur in the case of an accidental spill from a large volume transportation ship or storage tank became an area of concern. Such an event would create a low lying unconfined cloud of vaporized LNG that would result in a fatal and destructive explosion if it encountered a suitable ignition source. It was commonly held that a deflagration to detonation transition (DDT) of such mixtures was unlikely due to the inability of a flame to necessarily accelerate in an unbound environment. The ability to initiate detonations by direct (high explosive) [2,3] methods and the limiting propagation conditions were unknown. Numerical studies [3] were performed to estimate the critical mass of high-explosive needed to detonate CH_4-air mixtures and enormous values (1-10 tonnes) were predicted.

Experimental studies by Bull [4] using CH_4 were extrapolated to air conditions and suggested that a minimum mass of 22 kg of high explosive was needed to detonate a cloud. Benedict performed [5] large-scale (20 m^3) unconfined tests and found that about 4 kg of high explosive in a planar configuration was sufficient to establish stable detonations that would propagate at least 12 m. Given the large initiation energies and volumes of gas apparently required to obtain detonation, this was presumed unlikely to occur in concert with an accidental spill, assuming the gas cloud was only fueled by CH_4. However, it was also apparent from testing and modeling that the heavier alkanes present in natural gas, primarily ethane, play a crucial role in sensitizing the vapor cloud to direct initiation. Vander Molen and Nicholls [6] varied the CH_4 to C_2H_6 ratio in a stoichiometric (with air) unconfined cloud experiment and found that a fuel mixture composed of just 1% C_2H_6 by volume drastically decreased the critical initiation en-

M. D. Frederick
mfrederick@purdue.edu

R. M. Gejji
rgejji@purdue.edu

J. E. Shepherd
joseph.e.shepherd@caltech.edu

C. D. Slabaugh
cslabau@purdue.edu

ergy required to detonate the mixture. A similar study was performed by Bull, Elsworth, and Hooper [7] who found that a cloud with 10% ethane by fuel volume was seven times more detonable than one fueled by methane alone. A recent review [8] of unconfined vapor cloud explosions, identifies one known accidental explosion (Skikda, Algeria 2004) of a large vapor cloud containing natural gas that may have resulted in a detonation although a refrigerant and higher hydrocarbons may have been present in the cloud. The potential for unconfined vapor cloud detonation of methane or natural gas remains unresolved.

In order to identify the kinetic mechanism responsible for the increased detonability of multi-component fuels, such as LNG, Westbrook [9] developed a 75-step methane-ethane oxidation mechanism to numerically investigate the effect of ethane addition on the ignition delay time of CH_4-O_2-Ar mixtures. After finding good agreement with the shock-tube studies of Burcat, Scheller, and Lifshitz [10] for single component fueled mixtures (CH_4 and C_2H_6), Westbrook determined that the addition of up to 10% ethane by fuel volume into the mixture sensitizes the ignition delay to such a degree that LNG cannot be modeled accurately in the absence of ethane and higher alkanes. Westbrook and Haselman[11] then applied this model to computationally explore the detonability of vaporized LNG clouds in air for various ratios of methane to ethane and compared their results to the experimental results Bull et al. [7,12], finding good agreement. They concluded that the kinetic mechanism responsible for mixture sensitization is that atomic hydrogen, which is required to initiate chain branching reactions, is more readily abstracted from ethane than from methane. Moreover, the oxidation of methane does not immediately produce hydrogen radicals, rather it proceeds through ethane. This effect holds for other alkane fuels, all of which do not bind hydrogen as strongly as methane. More recently Lamoureux et al. [13,14] developed an empirical correlation using methane, ethane, and propane to determine the ignition delay time of natural gas behind reflected shocks and found good agreement with an updated detailed kinetic mechanism. They reached similar conclusions to Westbrook: accounting for the higher hydrocarbons in natural gas is critical in understanding its detonation properties.

In addition to the direct initiation of an unconfined gas-cloud relevant to LNG spills, there is a safety concern with the detonation of natural gas-air mixtures through DDT in confined environments, namely underground coalmines. If enough natural gas escapes a coal seam to create a flammable mixture any accidental ignition could result in a detonation. The coal mine tunnels are often large in diameter (2 m), several kilometers long, and have rough walls and obstacles that may promote flame acceleration. All of these conditions are known to be factors in initiating detonation through DDT. Several studies [15–18] have considered this problem and determined that DDT is possible in such environments and have suggested risk mitigation steps for existing mines.

The development of rotating detonation combustor (RDC) technology presents an interesting perspective change toward detonable mixtures. Where detonation avoidance is paramount from a safety viewpoint for LNG transport and mining operations, RDCs may benefit from mixtures that are more detonable. Recent RDC studies have investigated fuel-air mixtures where the fuel is a blend of hydrogen and methane/natural gas [19–22]. These studies show that the presence of hydrogen in the fuel has a distinct effect on the combustor performance. However, the results are not conclusive as to what ratio is most beneficial. Achieving an operable RDC requires a balance of chemical kinetics, injector dynamics, operating condition, and combustor dimension. None of these variables can be decoupled from each other and optimization is often device-specific. A more detonable mixture may be better for some RDCs and worse for others, making a broad claim about desired mixture detonability is not possible at this time.

The present study examines the characteristics of propagating detonations within methane and natural gas-oxygen-diluent mixtures in laboratory tests. The primary objective is to characterize the structure of the detonation front in methane and natural gas mixtures diluted with 25% and 33% nitrogen with the use of simultaneous time-revolved schlieren and CH^* chemiluminescence imaging. This is accomplished using high-repetition rate, high-resolution imaging systems to obtain and analyze the dynamic structure of planar detonations. We observe and characterize the effects of dilution and the addition of heavier alkanes to CH_4 on detonation front structure.

2 Experiment Description

2.1 Detonation Channel

The *Narrow Channel Facility* (NCF) was developed at the Explosion Dynamics Laboratory at Caltech [23] and used to characterize detonation front structure using various imaging techniques [23,24]. The NCF was transferred and integrated with the experimental infrastructure at Zucrow Laboratories at Purdue University for this study [25,26]. The NCF is a rectangular channel with a height of 152.4 mm and width of 17.78 mm. The

dimensions were chosen such that the width is nominally smaller than the dominate detonation cell size for a targeted range of mixtures and test conditions. This configuration effectively suppresses transverse wave motion across the width of the channel, generating a nominally two dimensional detonation structure across the channel height. The small-scale structure of the detonation front is still three-dimensional but the large amplitude transverse waves move perpendicular to the line of sight, a situation that is favorable for the application of planar (and path-integrated) optical diagnostics.

The NCF is 4.2 m long and has 170-mm-diameter optical windows located near the end of the channel for visualization of the detonation. Figure 1 shows an overview of the experiment. The reactants are introduced into the channel using the method of partial pressures. The chamber is initially purged with the diluent gas (typically N_2 or Ar) used in the test, then drawn to a pressure of 3.5 kPa using a vacuum pump. The fill process begins with introduction of the diluent gas into the chamber until the partial pressure corresponds with the prescribed mole fraction for the test. The same procedure is used to fill fuel and oxidizer into the channel, with a short delay between the introduction of each new reactant to allow for an average measure of pressure to be obtained. The mixture is circulated throughout the loading process to homogenize the reactants. Once the reactants are at the target initial pressure and mixture conditions in the channel, they are circulated for an additional thirty seconds prior to initiation. The loading processes takes approximately two minutes and the leak rate of ambient air into the chamber during this time is $\sim$7 Pa/min, which has a negligible effect on the desired mixture composition. The planar detonation is driven by a branched initiator, designed by Jackson and Shepherd [27]. The initiator operates with an equimolar C_2H_2-O_2 mixture and is ignited with a spark plug. Following a rapid deflagration-to-detonation transition (DDT), the initial detonation is split into a symmetric network of channels that divide it into sixteen wavefronts, distributed across the height of the channel. The waves quickly merge to produce a planar detonation within the channel that propagates into the test gas. The system is vented of all product gases and purged with an inert gas at the completion of the test.

2.2 Reactant Supply System

Reactant circuits have been configured to allow for control of the propellant loading process from up to seven independent sources: three fuels, two oxidizers, and two inert gases. Specific consideration was given to the need for accurate and repeatable loading of small quantities of gas, approximately three grams per test. All circuits are isolated from the NCF with pneumatically actuated ball-valves. An orifice is installed immediately downstream of each valve to restrict the flow rate. The supply pressures are regulated to ensure that the fill rate is sufficiently low for robust control with the resolution of the pneumatic valve actuation time. The reactant loading process is automated and takes approximately 120 s, depending on the test condition. All cases presented in this work were repeated to within 1.3% variance of the desired mixture composition.

2.3 Measurement Systems

Reactant introduction for both the detonation channel and the branched initiator is monitored by GE Druck UNIK 50E6 pressure transducers. Each pressure transducer is accurate to within $\pm$0.055 kPa. A K-type thermocouple is placed just upstream of the branched initiator entrance and is used record the pre-detonation temperature. These instruments are sampled at 1 kHz and are recorded with a National Instruments DAQ. The pressure and temperature instrumentation is isolated from the channel prior to detonation.

Pressure fluctuations in the channel are recorded at five axially distributed locations using PCB 113B26 dynamic pressure transducers (PT), installed flush with the channel wall, and sampled at 2 MHz. PT 1-3 monitor the planarity of the wave as it enters the test section. PT 4-7 are used to track the progression of the detonation wave as it traverses the channel by using the time of arrival method. Figure 1 identifies the location of all the HF measurement locations (PT 1-7).

Simultaneous 175-kHz schlieren and CH^* chemiluminescence are used to obtain spatial information about the density and reaction field, respectively. Figure 2 shows the optical setup and imaging field of view. In order to minimize motion blur without the use of an external gating device, the CAVILUX Smart UHS pulsed light source is used for the schlieren measurements. The CAVILUX produces incoherent 640 $\pm$ 6-nm light with a 10-ns pulse duration. An aspheric condenser lens is placed directly downstream of the light source and a series of lenses are used to set the divergence angle of the light, defined by the desired field of view and focal length of the parabolic mirror, before passing the focus of the beam through an aperture to enforce a point source. Parabolic mirrors with f/10 are used to collimate and direct the light through the test section. A 640/20-nm single-band bandpass filter (Semrock FF01-640/20 BrightLine) in front of the camera is used to eliminate light emission from the detonation. A circular aperture is used as the schlieren cut-

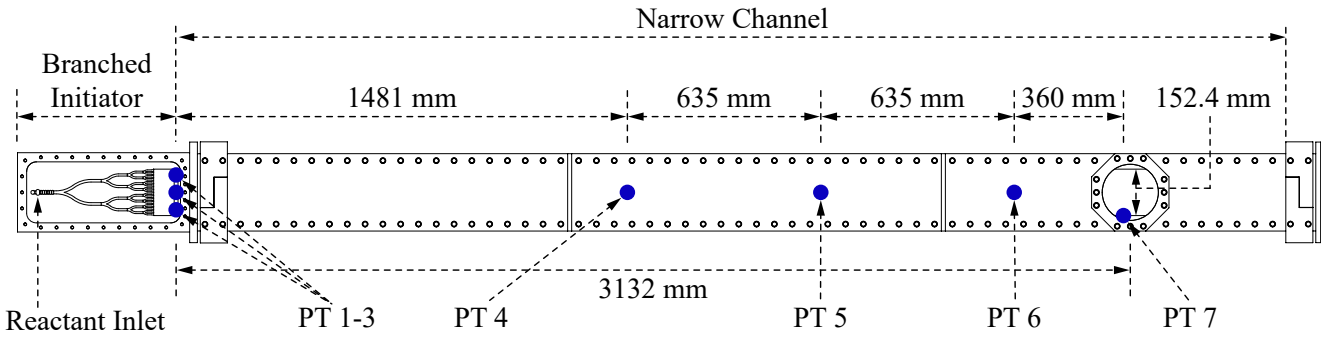

Fig. 1 Rendering of experimental facility with key dimensions indicated. Pressure measurement locations are labeled as PT1-PT7.

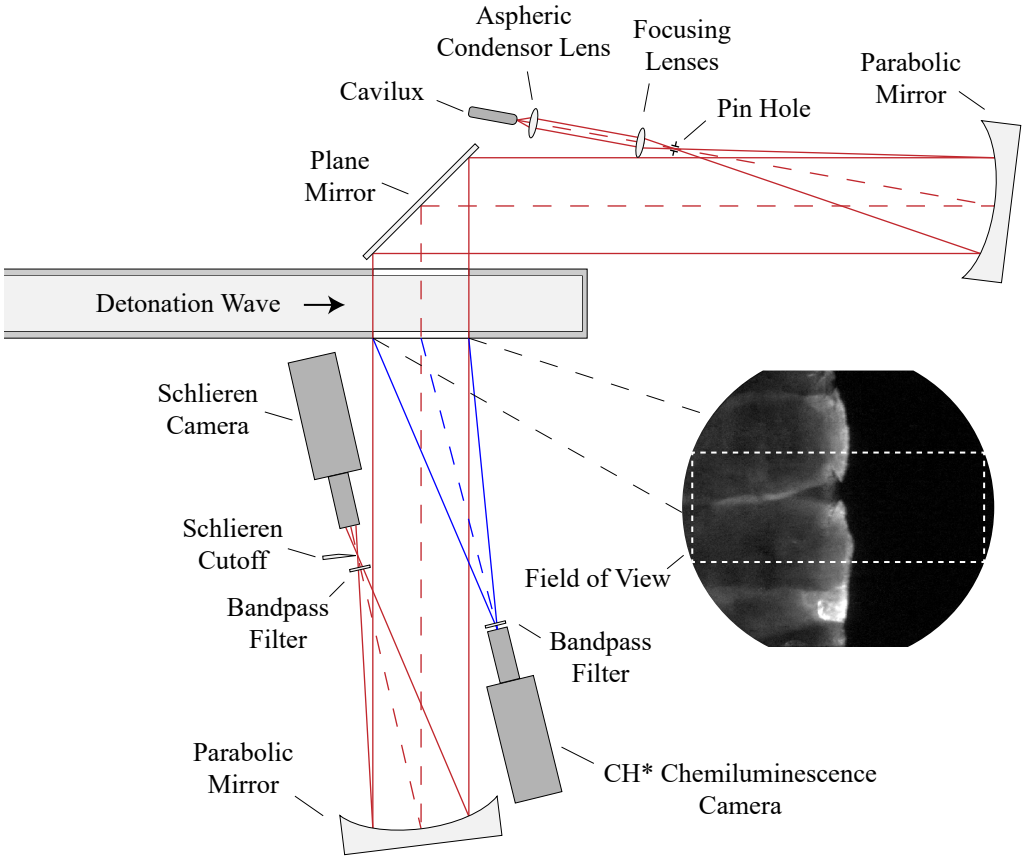

Fig. 2 Schematic illustration of optical configuration for simultaneous schlieren and CH* chemiluminescence measurements. Not to scale.

off. The resulting image is recorded on a Photron SA-Z CMOS camera. Background subtraction is performed on the schlieren images to eliminate the appearance of window defects. An image acquired before the detonation wave enters the field of view is used as the background. The CH* chemiluminescence ($A^2\Delta \rightarrow X^2\Pi_r$) is recorded on a Phantom V-2512 with a 1-μs exposure and using a 434/17-nm (Semrock 434/17 BrightLine) single-band bandpass filter in front of the camera. The optical axis of this camera is offset by 10° from normal incidence with the window and the resulting images are projected onto the normal plane. The overlapping field of view between schlieren and chemiluminescence images is 160 × 60 mm, depicted in Figure 2.

OH* chemiluminescence commonly presents stronger signal in turbulent flames than CH* [28,29]. However, the CH* radical spontaneously emits at 431 nm, which is within the spectral range of the Phantom V-2512, and produces enough signal to be imaged. This eliminates the need for a UV-sensitive intensifier, which is required to capture the OH* spontaneous emission at 309 nm. Some chemiluminescence from excited CO_2 and C_2 will

be transmitted by the 434-nm filter but these only contribute a minor amount to the overall signal [30–32].

The spatial distribution of the mole fractions of CH* and OH* are estimated using the one-dimensional idealized ZND model of a detonation of CH_4-$2O_2$-N_2 at 22.9 kPa and 290 K. The simulation used the GRI 3.0 reaction mechanism [33] with the addition of the OH* and CH* submechanisms from Nori et al. [31] and thermodynamic data valid for detonation conditions. Computations using the FFCM1 mechanism [34] show similar results. As shown in Figure 3, the mole fraction of both species have similar orders of magnitude, with CH* having a slightly larger spatial extent and the peak occurring closer to the maximum thermicity location than for OH*. The ZND model does not take into account velocity oscillations of the lead shock or self-absorption of the spontaneous emission and therefore can only be use to qualitatively compare with experimental results. A comparison of representative OH* and CH* images is shown in Figure 4. The OH* image was taken with a Lambert HiCATT 25 UV intensifier coupled to the Phantom V-2512. Both images presented in Figure 4 are of a CH_4-$2O_2$-N_2 detonation with $P_0 = 22.9$ kPa and $T_0 = 290$ K. The CH* images display significantly larger dynamic range and enhanced resolution of the smaller spatial scales within the detonation front, features that are not visible in the OH* chemiluminescence images using an intensifier. The relative intensity of the signal cannot be compared, as the two images were taken with different imaging systems.

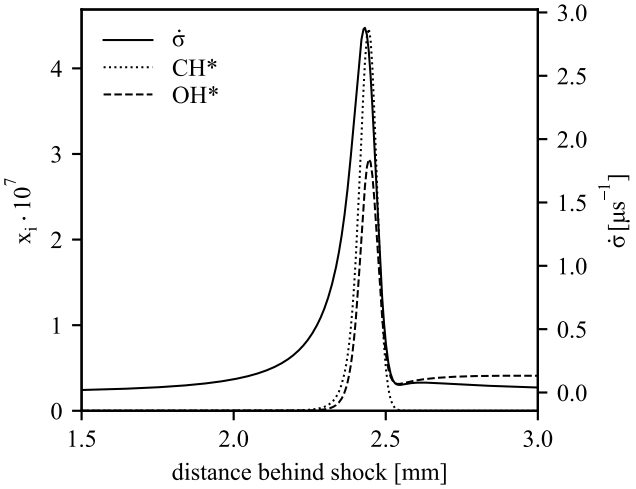

Fig. 3 Mole fraction x_i of excited species CH*, OH*, and thermicity $\dot{\sigma}$ of a CH_4-$2O_2$-N_2 ZND detonation. $P_0 = 22.9$ kPa, $T_0 = 290$ K.

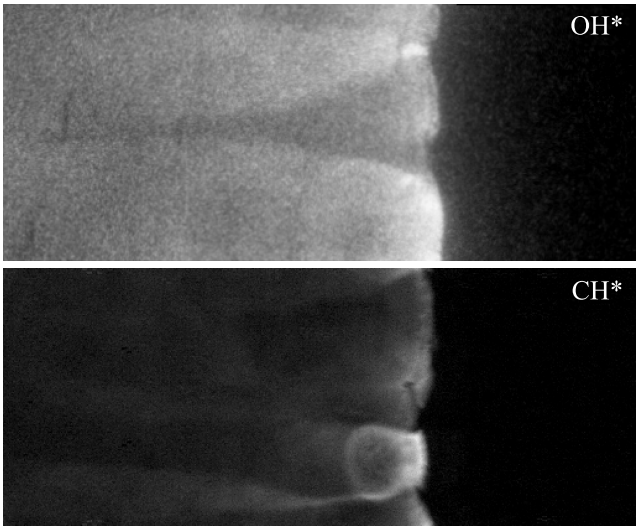

Fig. 4 Typical single-frame chemiluminescence images acquired in a CH_4-$2O_2$-N_2 detonation: OH* (top) and CH* (bottom).

3 Results and Discussion

Methane and natural gas were studied in this work with varying level of nitrogen dilution. The conditions are presented in Table 1. A stoichiometric mixture of fuel and oxygen was burned with 25% and 33% nitrogen dilution. The methane composition was reported by the vendor to be 99% pure. The natural gas composition was measured using an MKS MultiGas 2030 FTIR gas analyzer to be 92.4% CH_4, 6% C_2H_6, 1% N_2, 0.3% C_3H_8, and 0.3% CO_2. The initial pressure and temperature for all cases was held constant at $P_0 = 22.9$ kPa and $T_0 = 290$ K. The detonation parameters shown in Table 1 are calculated for an ideal ZND detonation using the Shock and Detonation Toolbox [35]. The reported table values are the Chapman Jouguet velocity (U_{CJ}), the von Neumann temperature and pressure (T_{vN} and P_{vN}), the Mach number (M_{CJ}), the induction length (Δ_I), the exothermic length (Δ_E), and the reduced effective activation energy (θ).

The detonation front speed was estimated by using the difference in time of arrival between pressure transducers. The speed as a function of downstream distance is normalized by the theoretical detonation velocity U_{CJ} and shown in Figure 5. Each condition was repeated once. The points correspond to the axial location of transducers 4-7, shown in Figure 1. The normalized wave speeds in this work fluctuate between −5% and 6% of U_{CJ}, but tend toward being slightly over-driven. Data from transducers 1-3, not plotted, show that the initiator wave front arrives at this location with less than 1-μs time difference across the height of the chan-

Table 1 Calculated detonation parameters at $P_0 = 22.9$ kPa and $T_0 = 290$ K [35].

Case	Mixture	U_{CJ} [m/s]	T_{vN} [K]	P_{vN} [MPa]	M_{CJ}	Δ_I [mm]	Δ_E [mm]	Δ_I/Δ_E	θ
a	CH_4-$2O_2$-N_2	2166	1743	1.07	6.20	2.43	0.106	22.9	11.22
b	CH_4-$2O_2$-$1.5N_2$	2111	1716	1.02	6.04	3.45	0.132	26.1	11.55
c	NG-$2O_2$-N_2	2167	1747	1.09	6.25	1.24	0.103	12.0	10.71
d	NG-$2O_2$-$1.5N_2$	2114	1721	1.03	6.09	1.69	0.133	12.7	11.01

nel, confirming that a nominally planar wave is initially generated by the branched initiator.

3.1 Structure of Detonation

The structure of unstable detonation fronts has been described in many previous studies and will only be briefly reviewed here. The structure consists of an unstable leading front that spatially and temporally oscillates due to the coupling with the reaction zones and transverse waves behind the front. These oscillations are associated with rapid acceleration after collision of transverse waves of the opposite family followed by decay of the leading shock until the next transverse wave collision. Superposed on this semi-regular structure are fine scale motions from a variety of sources including shear layers originating at the triple points at the intersection of the transverse wave and leading shock. The leading shock geometry, transverse waves, and triple points can be observed in Figure 6 along with substantial small scale structure typical of detonations in hydrocarbon mixtures.

In the initial phase of acceleration and decay of the high-speed regions of the leading front, the geometry resembles that of Mach reflection [36,37] in non-reacting gases. The high-speed portion of the leading shock front is often referred to as Mach stem and neighboring slower portion as the incident shock, although the roles of the two portions of the wave fronts are reversed as the high-speed portion of the wave decays to a low speed. Transverse waves are observed entering in from the top and bottom of frames CL.4-7 of Figure 6, which presents simultaneous schlieren and CH^* chemiluminescence images of case (b). Gases processed by the high-speed portions of the leading front at the top and bottom of these frames are rapidly burned and appear as regions of higher brightness along the front. Gases processed by the lower speed portions of the leading shock in the center of these frames react slowly and little or no intensity is seen in the chemiluminescence images. The transverse waves move laterally within the channel and show slightly higher chemiluminescence compared to the surrounding gas. When transverse waves collide, as in frame 8, high intensity chemiluminescence is observed, indicating rapid reaction, which results in the rapid acceleration of the leading front. Transverse waves propagate outward (frames 9-12) from the collision region, interact with other waves, and reflect from the upper and lower walls of the channel to re-initiate the cycle of oscillation of the leading front. Each wave cycle traces out a detonation cell that is bounded by the path of the two triple points that border the leading shock of the cell. The tallest point in the cell cycle, which occurs when neighboring high speed shocks form, is defined as the cell size λ. This is most easily illustrated using a soot foil [23].

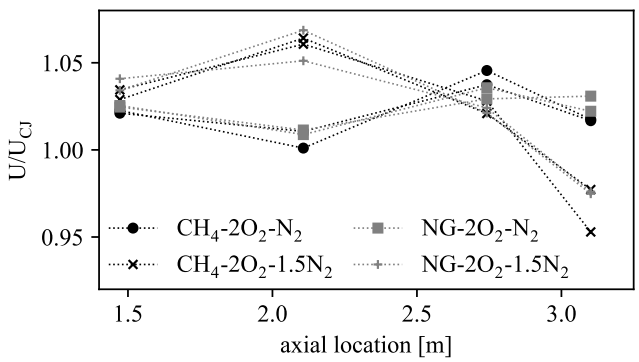

Fig. 5 Normalized axial wave velocity of all mixtures in Table 1, each repeated once.

Frame CL.6 shows a characteristic feature of unstable detonations, known as a "keystone" [38], in which a pocket of unburned reactants exists behind the leading front and is surrounded by burning reactants and products. Keystones form because of the large fluctuations in lead shock velocity, ranging between $0.75 < U_{local}/U_{CJ} < 1.5$ in unstable detonations [39–41]. Behind the low-speed shock (incident shock), the induction length becomes large because the reactants are processed by a weak shock, relative to the high-speed shock (Mach stem). The region of decreased chemiluminescence intensity behind these low speed regions is observed to be as large as 60 mm in this work (see frame b1 of Figure 8). On the other hand, reactants that are processed by a high-speed shock, shown clearly along the center of the leading front in frames 9 through 12, have high-intensity reaction fronts that begin much closer to the leading shock, perhaps within 1 mm or less.

We have used the highly-idealized one-dimensional (Zel'dovich-von Neumann-Döring or ZND) detonation

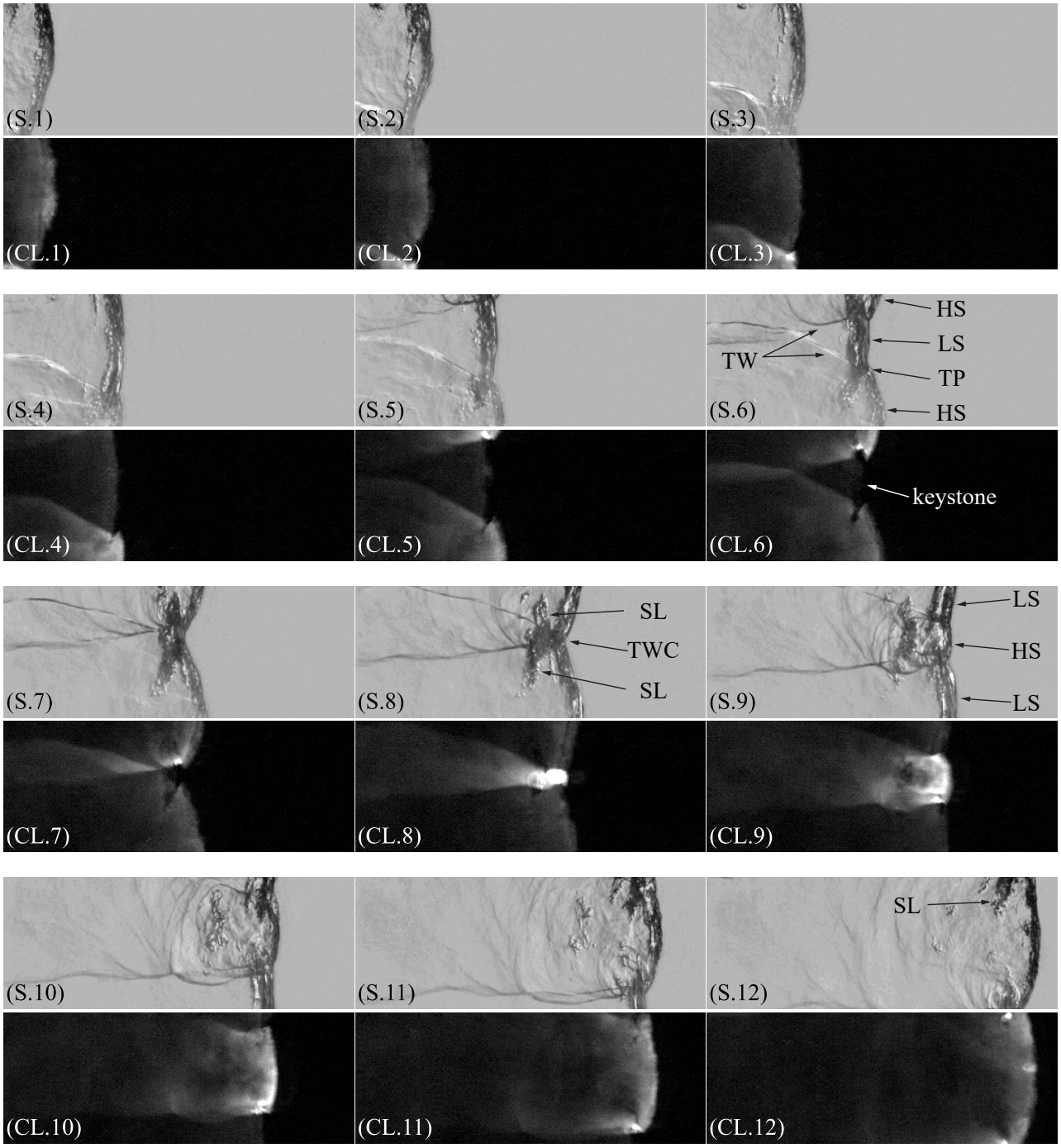

Fig. 6 Simultaneous schlieren (top row) and CH* chemiluminescence (bottom row) images of a CH_4-$2O_2$-$1.5N_2$ detonation. The time between images is 5.71 μs and the size of each image is 160×60 mm. Select images are labeled with: HS: high-speed region, LS: low-speed region, TW: transverse wave, SL: shear layer, and TWC: transverse wave collision.

model to provide estimates of the reaction zone properties. The ZND model predicts a reaction zone that extends 1-4 mm behind a shock front propagating at the CJ speed, see Δ_I in Table 1. The four cases (a, b, c, d) correspond to the main mixtures examined in the present study. Case (b) of Table 1 corresponds to the mixture of Figure 6. The initially high-speed leading shock front is decaying in frames 1-3. As the wave decays, transverse waves arrive from the top and bottom of the frame and following the intersections and explosion in frames 8-9, the high-speed (Mach stem) portion

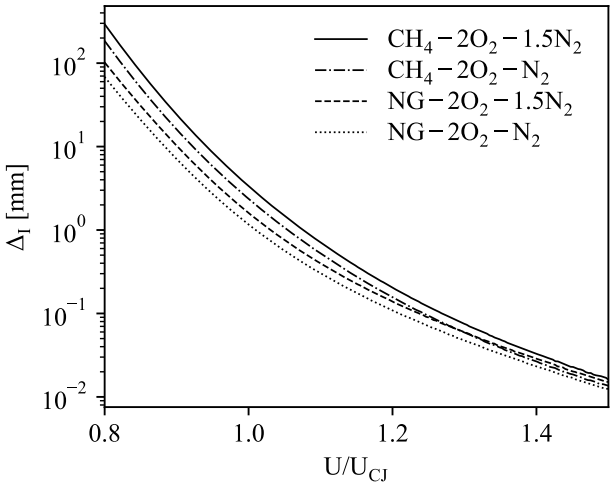

Fig. 7 Induction length variation as a function of normalized lead shock speed calculated using the constant-pressure model.

of wave can be observed to expand and decay in frames 10-12.

Of course, the estimates of Table 1 are only notional, the reaction zone length and time scales vary drastically with the leading shock front oscillations. Figure 7 shows the range of induction lengths that can be anticipated as a function of lead shock speed. These values are calculated using a one-dimensional, steady, and adiabatic constant-pressure model [35]. The constant-pressure model is used for these computations because use of the ZND model results in a singularity as the shock velocity falls below U_{CJ}. The constant-pressure simulation gives results that are within 5% of ZND simulations for values of $U > U_{\mathrm{CJ}}$. Comparison was also made using the constant-volume simulation, but the constant-pressure simulation results in better agreement with ZND for computation of Δ_{I}. This result was also obtained by Chatelain et al. [42] for a similar mixture. The range of induction lengths plotted in Figure 7 is about 100 mm and this is of the same order of magnitude as the length of the keystone pockets that can be observed in Figure 6.

Pairs of shear layers can be seen developing in frames S.4 - S.8 and S.9 - S.12 of Figure 6. The shear layer begins forming (frame S.2 and S.9) soon after a transverse wave collision. The keystone feature enlarges and is bounded by the paths of the triple points. Following transverse wave collision, the shear layer detaches at the point of collision (frames S.9 - S.11) as the lead shock accelerates forward (Mach stem). New shear layers form as the role of the leading shocks reverse and the cell cycle begins again. The top shear layer in frame S.12 shows evidence of the Kelvin-Helmholtz (KH) instability, which has been reported to manifest along these shear layers in other work [38,43,44].

3.2 Effects of Dilution

A change in the concentration of nitrogen diluent in these mixtures has a marked effect on the detonation structure. Figure 8 shows a selection of consecutive CH^* chemiluminescence frames from methane denotations with 25% (left column) and 33% (right column) dilution, cases (a) and (b) respectively. Immediately apparent is the difference in the dominant cell width λ between the two cases. The dominant cell width is about 37 mm for the less dilute case (case a) and 50 mm for the more dilute case (case b). The ratio of these widths is 0.74 and this agrees well with the ratio of induction lengths for the two cases, which is 0.70 (Table 1). The concurrence of the ratios follows from the simple empirical relation, $\lambda = \mathrm{A_I}\Delta_{\mathrm{I}}$ (A_I is an experimentally determined constant) that has been used in previous studies to predict cell size [45,46]. In the absence of quantitative theory, estimates of detonation parameters based on values computed from detailed kinetic mechanism, such as Δ_{I}, are convenient. Other such parameters that have been used to describe the stability of detonations are the reduced effective activation energy θ [47,48] and the ratio of induction length to exothermic length $\Delta_{\mathrm{I}}/\Delta_{\mathrm{E}}$ [49].

In addition to the dominant cell, there are intermediate cell crossings that occur over a wide range of length scales. Frames a1 and a2 of Figure 8 capture the moments just before transverse wave collision of the dominant cell, shown in frame a3. An intermediate high-speed shock of much smaller spatial scale than the dominant cell is captured within the keystone pocket of frame a2 (feature i). This feature does not seem to propagate further, perhaps due to the leading shock and surrounding transverse waves consuming the upstream reactants first. In frames a3 and a4 the leading shock accelerates after transverse wave collision and in frame a5 a collision between the upward moving transverse wave and another transverse wave moving down from the top of the frame is observed (feature ii). This collision occurs over a small spatial scale. As seen in frame a6, this event proceeds to cause a split of the lead front by the generation of a weak transverse wave moving downward (feature iii). Analysis of the simultaneous schlieren images for this case show that the transverse wave dissipates quickly.

The magnified cellular structure of the 33% dilution case (case b) on the right of Figure 8 shows a highly non-uniform transverse wave collision and resulting explosion. Alternating layers of high and low

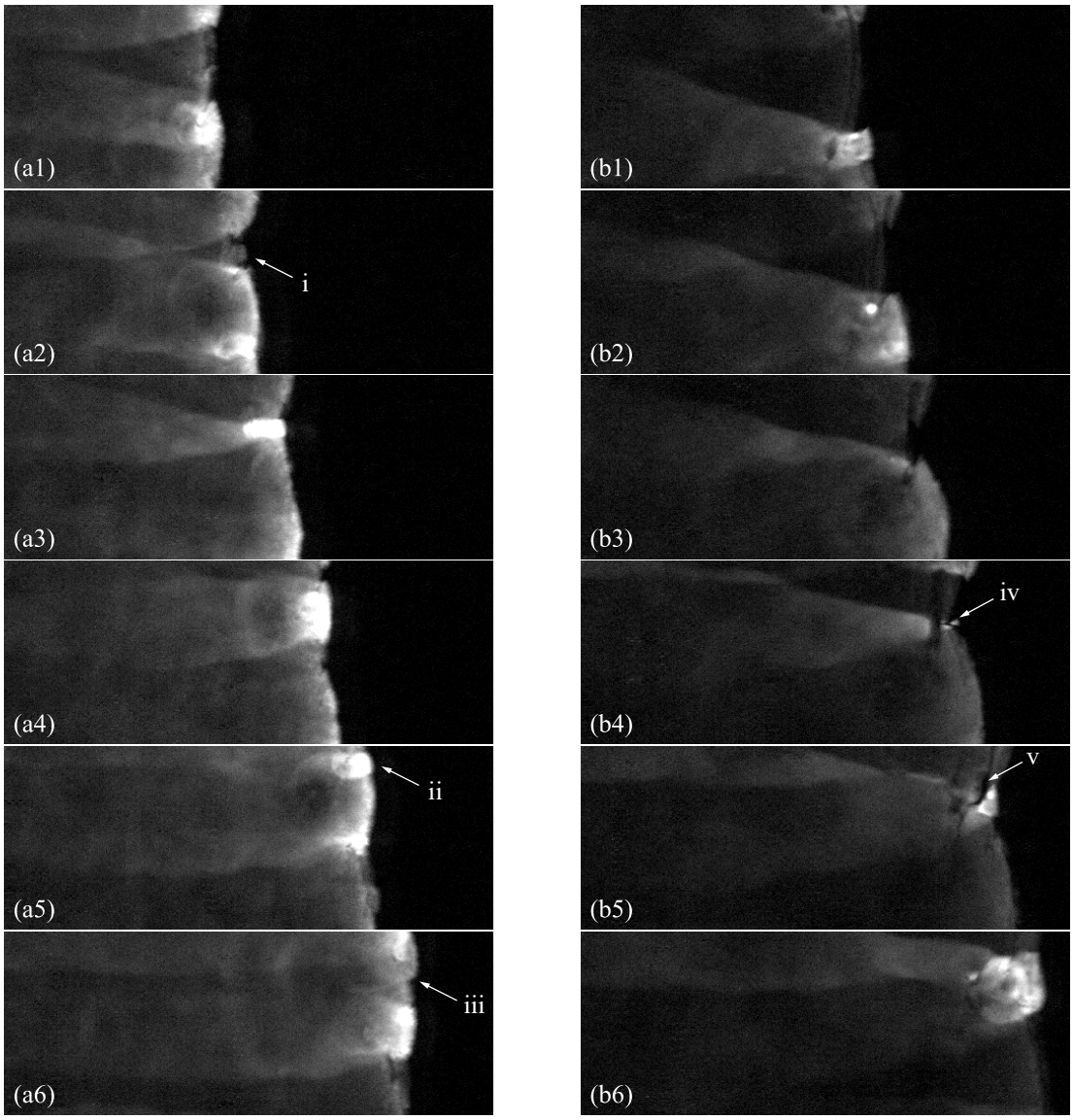

Fig. 8 CH^* Chemiluminescence of CH_4-$2O_2$-N_2 (case a, left) and CH_4-$2O_2$-$1.5N_2$ (case b, right). The time between images is 5.71 μs and the size of each image is 160 × 60 mm.

CH^* intensity are present as the transverse waves converge. The explosion that ensues following the transverse wave collision is spatially distributed. Frame b4 shows the first instance of accelerated burning (feature iv), as the transverse wave moving up from the bottom collides with the finger-like-structure moving down from the top. Burning intensifies as the most upstream portions of the leading shock front collide. In frame b5 pockets of unburned reactants (feature v) are evident behind a region of high-intensity burning and in frame b6 these unburned pockets are consumed in a highly non-uniform explosion.

Aside from the differences in the range of scales present for each case, there is also a marked difference in the intensity of the downstream region. The signal intensity in the 25% diluted case is much greater than the 33% diluted case, which is apparent when comparing the two cases in Figure 8. This observation holds for both methane and natural gas cases, which were studied with an identical detection system. One possible explanation for this behavior is that the reduced amount of nitrogen in the less dilute cases leads to less collisional quenching of the excited CH molecule. The ratio of maximum CH^* concentration calculated for a ZND detonation is $[CH^*_{33\%}]/[CH^*_{25\%}] = 0.59$ and the ratio of integrated intensity from 0 to 5 mm behind the leading front and along the entire height of the image for the frames shown in Figure 8 is $I_{33\%}/I_{25\%} = 0.56$.

Increasing the diluent percentage has implications for how the front burns reactants. For the case of 25% dilution (case a), burning is seen to occur over more of the lead front than in the 33% case. This occurs because the scales are smaller in the former case and this allows for more transverse wave collisions and therefore more high temperature regions to locally ignite reactants. For the more dilute case (case b), more reactants are processed by low-speed regions of the leading shock, which do not cause rapid burning. Instead, these large regions of near-zero reactivity create reactant pockets that, if ignited, generate highly non-uniform and spatially broad combustion events (seen in frame b6 of Figure 8). This increases the instability of the detonation and materializes a more stochastic cellular structure.

3.3 Comparison of Methane and Natural Gas Detonations

The introduction of natural gas, a multi-component fuel, produces a number of key differences in the detonation structure. Figure 9 compares the CH^* chemiluminescence of stoichiometric methane-oxygen and stoichiometric natural gas-oxygen, each with 25% nitrogen dilution and initiated at the same pressure and temperature (cases a and c). Both of these cases show complex front-structure, with features occurring over a wide range of spatial and temporal scales. Beginning with the pure methane case (case a), the lower half of frame a9 shows two strong transverse wave collisions that occur about 15 mm apart. The downward moving transverse wave generated by the upper collision (feature i) impacts the upward moving transverse wave originating from the lower collision (feature ii). The subsequent collision results in a region of high intensity 15 mm from the bottom of frame a10 (feature iii). This interaction traces out a small cell. However, the upward moving transverse wave generated by the upper collision (feature i) does not encounter a neighboring transverse wave so quickly and closes around the low-speed shock in the upper half of frames a9 and a10. This traces out a much larger cell.

The natural gas case (case c, right of Figure 9) presents large-scale spatial structure that is on the same order as the cell size of case (a), but also contains much smaller features. The leading front is not nearly as organized and instead burns in a more distributed fashion. Where discrete regions of high-intensity burning are seen in frames a4, a7, and a9 of case (a), case (c) shows similar intensity spread over the entire leading front. For example, frame c4 shows three small regions of high-intensity (feature iv) between two instances of transverse wave collision, indicating that high-intensity reactions are occurring along the decaying shock of the main mode of the detonation. In general the natural gas case also has a more continuous front. It does not have distinct shear layers separating reacted and unreacted gases, nor does it present large keystones, such as in frames a6 and a8.

In order to quantify the amount of burning that occurs along the lead front of cases (a) and (c), the probability distribution of normalized intensity is shown in Figure 10. The statistical set for each case is generated by extracting the measured chemiluminescence intensity from the leading edge to a location five millimeters behind it along the entire image height for all frames shown in Figure 9. This yields approximately 34,000 datapoints per case. The values are then normalized by the maximum intensity over the entire set for the corresponding case. The mean value for case (a) is 0.286 and the skewness is 1.189. The mean value for case (c) is 0.302 and the skewness is 0.493. The breadth of the distribution from case (c), relative to case (a), suggests that it contains a wider range of scales. The mean value of case (c) is shifted toward higher intensities, which supports the observation that case (c) has more intense burning along the leading front. The large value of skewness for case (a), as compared to case (c), tells us that the distribution has a large right-ward tail. In terms of intensities, this means that case (a) contains outliers that are extremely bright (transverse wave collisions). While, case (c) has fewer outliers along the leading front, which supports the observation that the high-intensity burning is more uniformly distributed.

The differences in the spatial-scales and spatial structure between these two test cases can be explained chemically, by the presence of ethane in the natural gas. As reported in the beginning of the results section, ethane only constitutes 6% of the natural gas, but has a marked effect on the spatial scales. For the cases shown in Figure 9, which are identical except for the fuel composition, the induction length Δ_I for case (c) (natural gas) is half that of case (a) (methane); 1.24 and 2.43 mm respectively (reported in 1). These calculations are similar to those of Westbrook and Haselman [11], who numerically compared the induction time of methane-ethane mixtures, but ours uses a much more recent chemical mechanism, GRI 3.0 high-temp. They found that the addition of 5% ethane into methane reduced the induction time of their mixtures by half, which is the same conclusion drawn by our simulations (see Figure 7).

To better visualize the scales introduced by ethane, Figure 11 shows a schlieren image of a C_2H_6-$3.5O_2$-$1.5N_2$ detonation with the same initial conditions as the other cases presented in this work. The one-dimensional

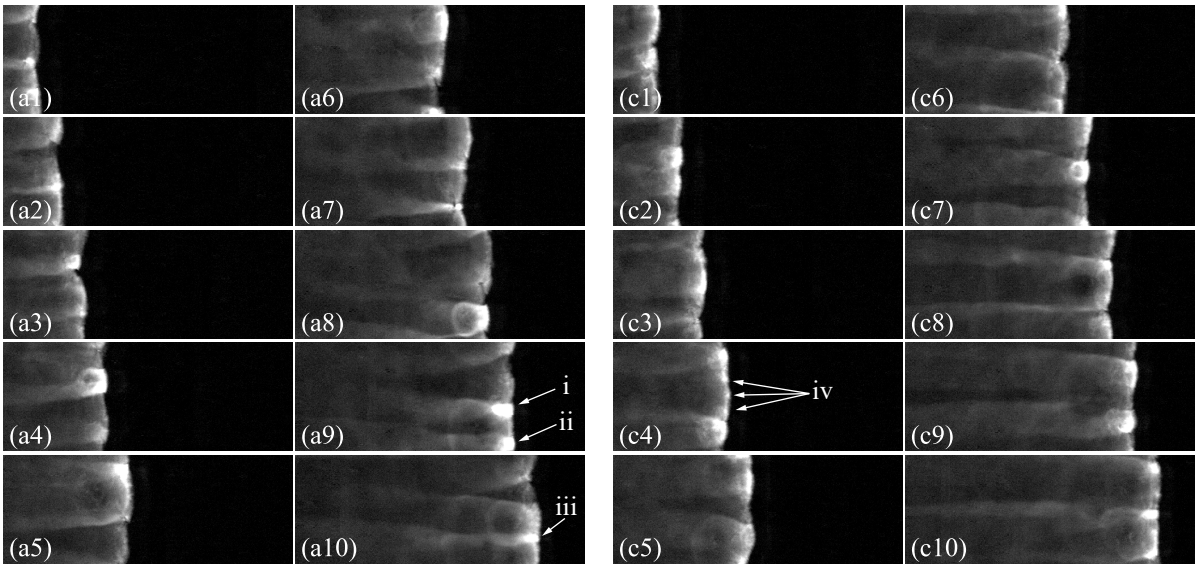

Fig. 9 CH* Chemiluminescence of CH_4-$2O_2$-N_2 (case a, left) and NG-$2O_2$-N_2 (case c, right). The time between images is 5.71 μs and the size of each image is 160 × 60 mm.

ZND induction length for this case is $\Delta_I = 0.321$ mm, almost 11 times smaller than the induction length for a methane detonation with the same level of dilution (case b). The much smaller cells that are allowed by pure ethane, the size of which is not resolvable by these measurements, moves the detonation toward a ZND-like one-dimensional structure. This has the effect of distributing regions of intense burning across the entire front because of the multitude of transverse wave collisions that are introduced, which each locally ignite reactants.

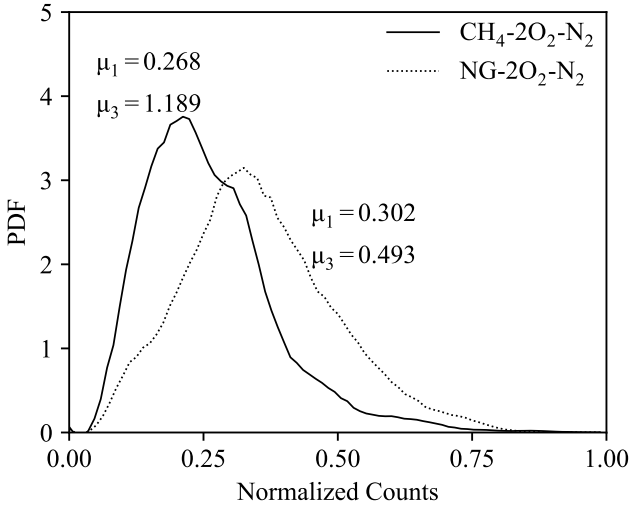

Fig. 10 Probability distribution of CH* chemiluminescence intensity along the leading fronts shown in Figure 9. The provided moments of distribution are μ_1: mean and μ_3: skewness.

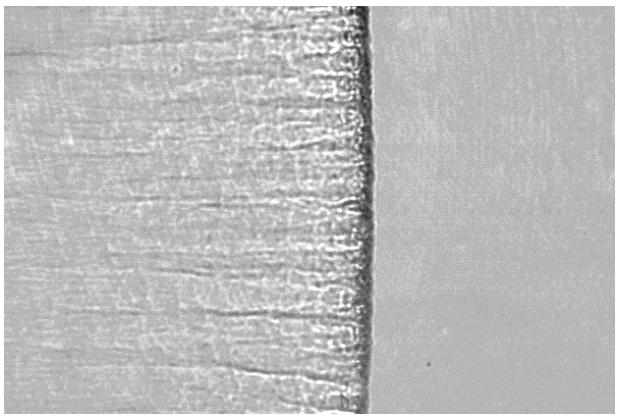

Fig. 11 Schlieren of C_2H_6-$3.5O_2$-$1.5N_2$ detonation. The size of the image is 61 × 41 mm.

In addition to modifying the burning that occurs along the front, the use of natural gas alters the structure of the detonation behind the leading front (as compared with methane). Figure 12 compares downstream features for methane case (b) (top) and natural gas case (d) (bottom); each has 33% nitrogen dilution. Each case captures the two frames before the transverse wave collision of the dominant cell mode and the three frames after the collision, after the shear layer detaches from the front. Throughout all frames there is a clear difference between the amount of wrinkling downstream of the front between cases (b) and (d). As the presence of ethane leads to smaller cell sizes and therefore more transverse wave collisions, the structure along the front becomes smaller and more wrinkled; the extreme of which is shown in Figure 11. The collision of two

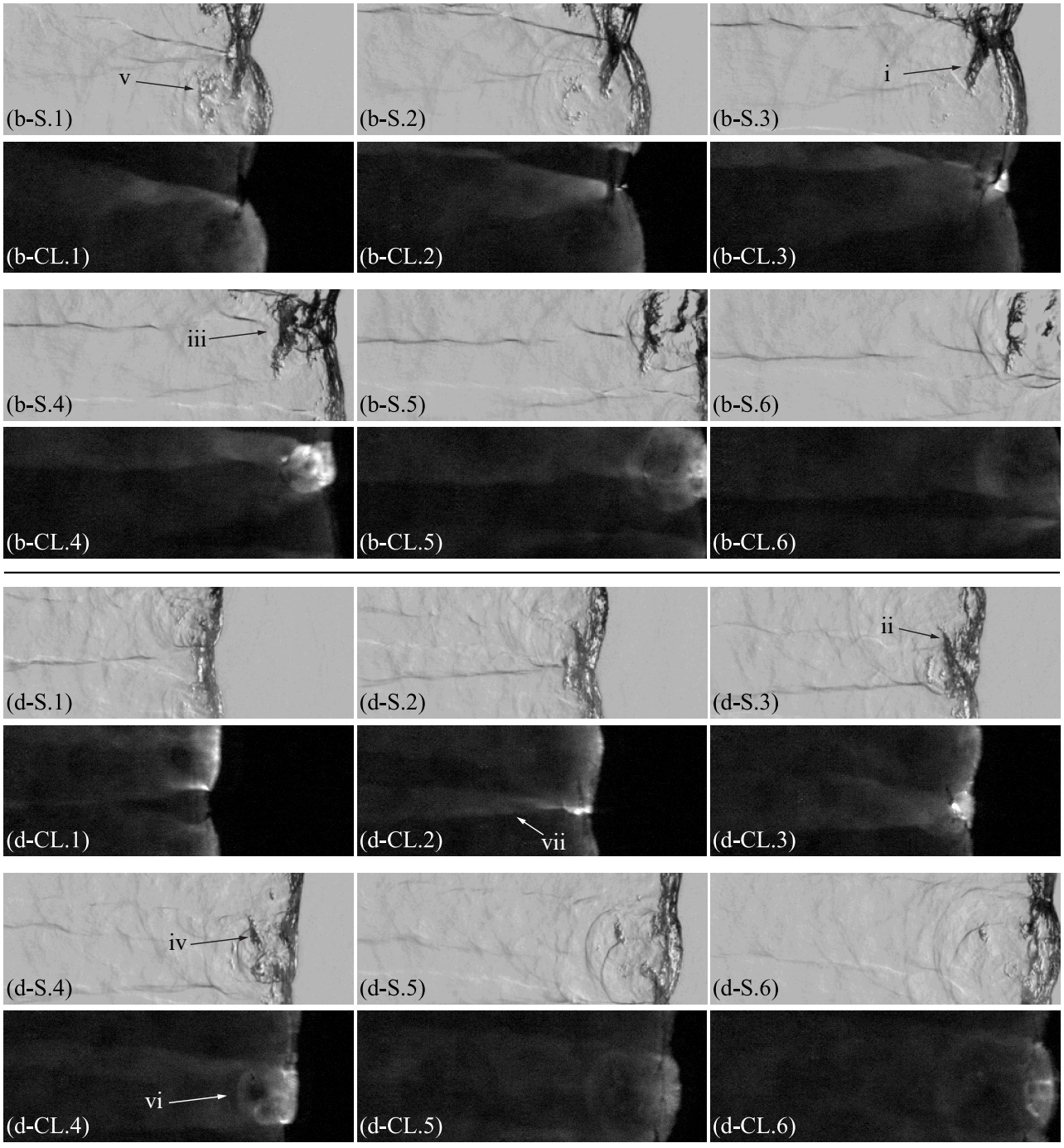

Fig. 12 Simultaneous schlieren (top row) and CH* chemiluminescence (bottom row) images of a CH_4-$2O_2$-1.5_2 detonation (case b) and NG-$2O_2$-$1.5N_2$ (case d). The time between images is 5.71 μs and the size of each image is 160 × 60 mm.

transverse waves serves as the source of a circular explosion, such as in frames S.9 - S.11 of Figure 6 for a single mode case. These circular explosions engender the increased wrinkling downstream of the leading front for case (d) as compared to case (b), because of the increased number of transverse wave collisions in case (d).

There is a distinct difference in shear layer formation and dissipation between cases (b) and (d). In frames b1 - b3 of Figure 12 a large shear layer, about 20 mm long in frame b-S.3 (feature i), forms as the transverse wave moves up from the bottom of the frame. However, for case (d), the largest shear layer that forms is only about 10 mm long (feature ii). These shear

layers separate reactants processed by the low-speed shock (incident shock), which are possibly unburned, and those processed by the high-speed shock (Mach stem), which quickly react. When the shear layers separate from the leading front, the material contained within, if unburned, may produce what has been termed an "unburned pocket" behind the front. This unburned pocket is not to be confused with the keystone of unreacted gas present behind the low-speed shock.

The first experimental observation of unreacted pockets was made by Subbotin [50] using schlieren measurements to study decaying $2H_2$-O_2-3Ar detonations and self-sustaining CH_4-$2O_2$-0.2Air detonations. Later, using OH planar laser-induced fluorescence imaging (PLIF), which allows for direct examination of the reaction field as opposed to schlieren, which requires interpretation of density variation, Austin [23,24] observed unreacted pockets in $2H_2$-O_2-xN_2 mixtures. Grib et al. recently imaged unreacted pockets in unstable hydrogen detonations using two-color PLIF [51]. Numerous computational studies have also been performed that observe the formation of unreacted pockets behind the front [38, 52–55]. The role that the consumption of these pockets plays in influencing the detonation front is important in understanding how the detonation is sustained. Any burning that occurs between the front and the hydrodynamic surface, which is the downstream surface at which the Mach number falls to unity, is capable of releasing energy that may feed, or otherwise influence, the front. The average hydrodynamic thickness (distance to the hydrodynamic surface) has been estimated, both through simulations and experiments, to be 4-7 λ [54, 56–58]. This leaves a large amount of space behind the front for the burning of unreacted pockets to influence the detonation.

Kiyanda and Higgins [59] used high-speed schlieren and broadband visible light imaging to estimate that in a stoichiometric methane-oxygen planar detonation 40% of the reactants processed by the leading shock within a cell cycle are transferred into a pocket behind the front. In examining how/if these pockets burn, the authors considered if adiabatic shock ignition from an incident shock or transverse wave was responsible. They determined that the induction time required for this method of consumption to occur is larger than what was experimentally observed for the pockets to fully dissipate from the schlieren images. The only mechanism that explained the speed of the pocket consumption and found good agreement with numerical simulations for their mixture was turbulent, diffusive burning [40, 53,54].

For the cases shown in Figure 12 there is clear separation of the shear layers, which may contain unburned reactants, from the leading front in frame b-S.4 and d-S.4 (features iii and iv, respectively). However, since the state and composition of gases within the shear layers has not yet been experimentally measured, we will refer to these pockets as detached shear layer volumes (DSLVs). The dissipation of the DSLVs behind the front occurs within about 40 mm for case (b) (λ = 60 mm) and 30 mm for case (d) (λ = 35 mm), which is 11.6 and 17.8 times the ZND induction length Δ_I at U_{CJ}, respectively. These dissipation lengths are less than or comparable to the estimated hydrodynamic length (4-7 λ). However, unlike the experimental observations of Kiyanda and Higgins, our chemiluminescence images in the current study do not show that the DSLVs behind the front are reactive. Frames b1-b3 show two stages of the DSLVs life cycle. The first stage is of the shear layer formation, as they are attached to the front (feature i). The second stage is a region of DSLVs, in the lower half of frame b1 and about 40 mm behind the front (feature v), that were generated from the previous cell cycle. None of these volumes show any indication of increased chemiluminescence as they dissipate. This holds true for the volumes in case (d), shown in the lower half of Figure 12, and for the repeat of case (b), shown in Figure 6. The only indication of increased light emission downstream of the front occurs along the circumference of the curricular explosions as they expand (feature vi, frame d-CL.4) and along the transverse waves, particularly when the transverse waves cross (feature vii, frame d-CL.2).

There are a number of reasons that may explain why we do not observe DSLV burning. First, if we assume that the density gradients behind the shock front are pockets of unburned reactants and that they do dissipate by turbulent deflagration it is possible that the chemiluminescence produced by this reaction is not detectable with our current system. While the CH^* radical is produced in super-equilibrium concentrations by shock-induced combustion, which is supported by 1D numerical simulations (Figure 3), the CH^* radical might not be produced in high enough concentrations by turbulent deflagration to be detected with our unintensified camera. Second, the transverse waves in these cases may be reactive and consume the unburned reactants that make it behind the front. The burning of reactants by a transverse wave is highly dependent upon the strength of that wave and on the strength of the portion of the leading shock that initially processes the reactants. Third, any unburned pockets that make it behind the front do not burn or undergo very slow reaction. However, it seems unlikely that if so many reactants were not contributing to the wave it would still propagate near CJ speed. Finally, it is possible that

the volumes that detach from the front do not contain unburned reactants at all and instead just consist of regions of products that exist within a fluid of much different density. This is plausible considering that the gas contained within the DSLVs was processed by a weak low-speed shock (incident shock) and the surrounding fluid was processed by a strong high-speed shock (Mach stem). These points all considered, the most likely variable governing the production and/or consumption of unburned pockets is the initial mixture composition and thermodynamic state. Only four cases with similar detonation parameters (see Table 1) were examined in this work. Exploring mixtures with higher or lower levels of dilution will likely reveal different DSLV formation and consumption behaviors.

4 Conclusions

The simultaneous time-resolved schlieren and CH^* chemiluminescence measurements present unique insight into highly-unstable hydrocarbon detonations. These results highlight the structural differences between methane and natural gas detonations and explain the increased detonability of natural gas mixtures. The use of CH^* chemiluminescence allows for a more accurate accounting of the reaction zone than visible light imaging, while also avoiding the deleterious effects of an image intensifier. Chemical kinetic simulations show that the introduction of ethane shrinks the spatial scales present in a detonation and experimental observations demonstrate how this distributes the burning along the leading front and reduces the size of the DSLVs. The smaller DSLVs that persist behind the front may increase the amount of reactants that burn upstream of the sonic surface and contribute to the sustention of the front. The lack of CH^* chemiluminescence from the DSLVs is surprising and suggests that interpretation of experimental schlieren images requires resolution of the accompanying reaction field to fully understand the flow field. A rigorous experimental effort to measure the composition of the DSLVs is needed to determine what role they play in sustaining the detonation.

Acknowledgments

Mark D. Frederick acknowledges support from the National Science Foundation Graduate Research Fellowship Program under Grant No. DGE-1333468. The high-speed camera used in this work was purchased with DURIP grant FA9550-16-1-0534 (Program Manager: Chiping Li).

Data availability

The datasets generated and analysed during the current study are available from the corresponding author on reasonable request.

References

1. Drake, E., Reid, R.C.: The importation of liquefied natural gas. Scientific American **236**(4), 22–29 (1977)
2. Lee, J.H.S.: Initiation of gaseous detonation. Annual Review of Physical Chemistry **28**(1), 75–104 (1977). https://doi.org/10.1146/annurev.pc.28.100177.000451
3. Boni, A.A., Wilson, C.W., Chapman, M., Cook, J.L.: A study of detonation in methane/air clouds. Acta Astronautica **5**(11), 1153–1169 (1978). https://doi.org/10.1016/0094-5765(78)90017-6
4. Bull, D.C., Elsworth, J.E., Quinn, C.P., Hooper, G.: A study of spherical detonation in mixtures of methane and oxygen diluted by nitrogen. Journal of Physics D: Applied Physics **9**(14), 1991–2000 (1976). https://doi.org/10.1088/0022-3727/9/14/009
5. Benedick, W.B.: High-explosive initiation of methane-air detonations. Combustion and Flame **35**, 89–93 (1979). https://doi.org/10.1016/0010-2180(79)90009-9
6. Vander Molen, R., Nicholls, J.A.: Blast wave initiation energy for the detonation of methane-ethane-air mixtures. Combustion Science and Technology **21**(1-2), 75–78 (1979). https://doi.org/10.1080/00102207908946920
7. Bull, D.C., Elsworth, J.E., Hooper, G.: Susceptibility of methane—ethane mixtures to gaseous detonation in air. Combustion and Flame **34**, 327–330 (1979). https://doi.org/10.1016/0010-2180(79)90106-8
8. Oran, E.S., Chamberlain, G., Pekalski, A.: Mechanisms and occurrence of detonations in vapor cloud explosions. Progress in Energy and Combustion Science **77**, 100804 (2020). https://doi.org/10.1016/j.pecs.2019.100804
9. Westbrook, C.K.: An analytical study of the shock tube ignition of mixtures of methane and ethane. Combustion Science and Technology **20**(1-2), 5–17 (1979). https://doi.org/10.1080/00102207908946891
10. Burcat, A., Scheller, K., Lifshitz, A.: Shock-tube investigation of comparative ignition delay times for C1-C5 alkanes. Combustion and Flame **16**(1), 29–33 (1971). https://doi.org/10.1016/S0010-2180(71)80007-X
11. Westbrook, C.K., Haselman, L.C.: Chemical kinetics in LNG detonations. In: Oppenheim, A.K., Manson, N., Soloukhin, R.I., Bowen, J.R. (eds.) Gasdynamics of Detonations and Explosions, vol. 75, pp. 193–206. American Institute of Aeronautics and Astronautics, New York (1981). https://doi.org/10.2514/5.9781600865497.0193.0206
12. Bull, D.C., Elsworth, J.E., Hooper, G.: Initiation of spherical detonation in hydrocarbon/air mixtures. Acta Astronautica **5**(11), 997–1008 (1978). https://doi.org/10.1016/0094-5765(78)90005-X
13. Lamoureux, N., Paillard, C., Vaslier, V.: Low hydrocarbon mixtures ignition delay times investigation behind reflected shock waves. Shock Waves **11**, 309–322 (2002). https://doi.org/10.1007/s001930100108
14. Lamoureux, N., Paillard, C.E.: Natural gas ignition delay times behind reflected shock waves: Application to modelling and safety. Shock Waves **13**, 57–68 (2003). https://doi.org/10.1007/s00193-003-0188-z
15. Zipf Jr., R.K., Gamezo, V.N., Mohamed, K.M., Oran, E.S., Kessler, D.A.: Deflagration-to-detonation transition in natural gas-air mixtures. Combustion and Flame **161**(8), 2165–2176 (2014). https://doi.org/10.1016/j.combustflame.2014.02.002
16. Zipf Jr., R.K., Gamezo, V.N., Sapko, M.J., Marchewka, W.P., Mohamed, K.M., Oran, E.S., Kessler, D.A., Weiss, E.S., Addis, J.D., Karnack, F.A., Sellers, D.D.: Methane-air detonation experiments at NIOSH Lake Lynn Laboratory. Journal of Loss Prevention in the Process Industries **26**(2), 295–301 (2013). https://doi.org/10.1016/j.jlp.2011.05.003
17. Oran, E.S., Gamezo, V.N., Zipf Jr., R.K.: Large-scale experiments and absolute detonability of methane/air mixtures. Combustion Science and Technology **187**(1-2), 324–341 (2015). https://doi.org/10.1080/00102202.2014.976308
18. Gamezo, V.N., Bachman, C.L., Oran, E.S.: Flame acceleration and DDT in large-scale obstructed channels filled with methane-air mixtures. Proceedings of the Combustion Institute **38**(3), 3521–3528 (2021). https://doi.org/10.1016/j.proci.2020.09.018
19. Bykovskii, F.A., Zhdan, S.A.: Continuous spin detonation of poorly detonable fuel-air mixtures in annular combustors. Journal of Physics: Conference Series **899**, 042002 (2017). https://doi.org/10.1088/1742-6596/899/4/042002
20. Bykovskii, F.A., Zhdan, S.A., Vedernikov, E.F.: Continuous detonation of methane/hydrogen-air mixtures in an annular cylindrical combustor. Combustion, Explosion, and Shock Waves **54**(4), 472–481 (2018). https://doi.org/10.1134/S0010508218040111
21. Roy, A., Bedick, C.R., Ferguson, D.H., Sidwell, T., Strakey, P.A.: Investigating instabilities in a rotating detonation combustor operating with natural gas–hydrogen fuel blend—effect of air preheat and annulus width. Journal of Engineering for Gas Turbines and Power **141**(11) (2019). https://doi.org/10.1115/1.4044980
22. Walters, I.V., Journell, C.L., Lemcherfi, A., Gejji, R.M., Heister, S.D., Slabaugh, C.D.: Operability of a natural gas-air rotating detonation engine. Journal of Propulsion and Power **36**(3), 453–464 (2020). https://doi.org/10.2514/1.B37735
23. Austin, J.M.: The role of instability in gaseous detonation. PhD thesis, California Institute of Technology (2003). https://doi.org/10.7907/X7YH-T687
24. Austin, J.M., Pintgen, F., Shepherd, J.E.: Reaction zones in highly unstable detonations. Proceedings of the Combustion Institute **30**(2), 1849–1857 (2005). https://doi.org/10.1016/j.proci.2004.08.157
25. Meyer, S.E., Heister, S.D., Slabaugh, C., Lucht, R.P., Pratt, A., Gejji, R.M., Bedard, M., Lemcherfi, A.: Design and development of the high pressure combustion laboratory at Purdue University. 53rd AIAA/SAE/ASEE Joint Propulsion Conference, Atlanta, GA, AIAA Paper 2017-4965 (2017). https://doi.org/10.2514/6.2017-4965
26. Slabaugh, C.D., Pratt, A.C., Lucht, R.P., Meyer, S.E., Benjamin, M., Lyle, K., Kelsey, M.: The development of an optically accessible, high-power combustion test rig. Review of Scientific Instruments **85**(3), 035105 (2014). https://doi.org/10.1063/1.4867084
27. Jackson, S.I., Austin, J.M., Shepherd, J.E.: Planar detonation wave initiation in large-aspect-ratio channels. AIAA Journal **44**(10), 2422–2425 (2006). https://doi.org/10.2514/1.21581
28. Nori, V.N., Seitzman, J.M.: CH* chemiluminescence modeling for combustion diagnostics. Proceedings of the Combustion Institute **32**(1), 895–903 (2009). https://doi.org/10.1016/j.proci.2008.05.050
29. Bedard, M.J., Fuller, T.L., Sardeshmukh, S., Anderson, W.E.: Chemiluminescence as a diagnostic in studying combustion instability in a practical combustor. Combustion and Flame **213**, 211–225 (2020). https://doi.org/10.1016/j.combustflame.2019.11.039

30. Miller, J.D., Peltier, S.J., Slipchenko, M.N., Mance, J.G., Ombrello, T.M., Gord, J.R., Carter, C.D.: Investigation of transient ignition processes in a model scramjet pilot cavity using simultaneous 100 kHz formaldehyde planar laser-induced fluorescence and CH* chemiluminescence imaging. Proceedings of the Combustion Institute **36**(2), 2865–2872 (2017). https://doi.org/10.1016/j.proci.2016.07.060
31. Nori, V.N.: Modeling and analysis of chemiluminescence sensing for syngas, methane and Jet-A combustion. PhD thesis, Georgia Institute of Technology (2008)
32. Gaydon, A.G.: The Spectroscopy of Flames. Chapman and Hall LTD., London (1957). https://doi.org/10.1007/978-94-009-5720-6
33. Smith, G.P., Golden, D.M., Frenklach, M., Moriarty, N.W., Eiteneer, B., Goldenberg, M., Bowman, C.T., Hanson, R.K., Song, S., Gardiner Jr., W.C., Lissianski, V.V., Qin, Z.: GRI-Mech 3.0. http://combustion.berkeley.edu/gri-mech/version30/text30.html
34. Smith, G.P., Tao, Y., Wang, H.: Foundational Fuel Chemistry Model Version 1.0 (FFCM-1) (2016). http://nanoenergy.stanford.edu/ffcm1
35. Shepherd, J.E.: Shock and Detonation Toolbox (2018). https://shepherd.caltech.edu/EDL/PublicResources/sdt/
36. Hornung, H.: Regular and Mach reflection of shock waves. Annual Review of Fluid Mechanics **18**(1), 33–58 (1986). https://doi.org/10.1146/annurev.fl.18.010186.000341
37. Ben-Dor, G.: Shock Wave Reflection Phenomena, 2nd edn. Springer, Berlin (2007). https://doi.org/10.1007/978-3-540-71382-1
38. Pintgen, F., Eckett, C.A., Austin, J.M., Shepherd, J.E.: Direct observations of reaction zone structure in propagating detonations. Combustion and Flame **133**(3), 211–229 (2003). https://doi.org/10.1016/S0010-2180(02)00458-3
39. Shepherd, J.E.: Detonation in gases. Proceedings of the Combustion Institute **32**(1), 83–98 (2009). https://doi.org/10.1016/j.proci.2008.08.006
40. Radulescu, M.I., Sharpe, G.J., Law, C.K., Lee, J.H.S.: The hydrodynamic structure of unstable cellular detonations. Journal of Fluid Mechanics **580**, 31–81 (2007). https://doi.org/10.1017/S0022112007005046
41. Frederick, M.D., Gejji, R.M., Shepherd, J.E., Slabaugh, C.D.: Statistical analysis of methane detonation wave structure in a narrow channel. AIAA Scitech 2021 Forum, AIAA Paper 2021-0800 (2021). https://doi.org/10.2514/6.2021-0800
42. Chatelain, K.P., He, Y., Mével, R., Lacoste, D.A.: Effect of the reactor model on steady detonation modeling. Shock Waves **31**, 323–335 (2021). https://doi.org/10.1007/s00193-021-01022-w
43. Austin, J.M., Shepherd, J.E.: Detonations in hydrocarbon fuel blends. Combustion and Flame **132**(1), 73–90 (2003). https://doi.org/10.1016/S0010-2180(02)00422-4
44. Massa, L., Austin, J.M., Jackson, T.L.: Triple-point shear layers in gaseous detonation waves. Journal of Fluid Mechanics **586**, 205–248 (2007). https://doi.org/10.1017/S0022112007007008
45. Westbrook, C.K.: Chemical kinetics of hydrocarbon oxidation in gaseous detonations. Combustion and Flame **46**, 191–210 (1982). https://doi.org/10.1016/0010-2180(82)90015-3
46. Shepherd, J.E.: Chemical kinetics of hydrogen-air-diluent detonations. In: Leyer, J.-C., Soloukhin, R.I., Bowen, J.R. (eds.) Dynamics of Explosions, pp. 263–293. American Institute of Aeronautics and Astronautics, New York (1986). https://doi.org/10.2514/5.9781600865800.0263.0293
47. Gavrikov, A.I., Efimenko, A.A., Dorofeev, S.B.: A model for detonation cell size prediction from chemical kinetics. Combustion and Flame **120**(1), 19–33 (2000). https://doi.org/10.1016/S0010-2180(99)00076-0
48. Schultz, E., Shepherd, J.E.: Validation of detailed reaction mechanisms for detonation simulation. Technical Report FM99-5, Graduate Aeronautical Laboratories: California Institute of Technology (2000)
49. Ng, H.D., Radulescu, M.I., Higgins, A.J., Nikiforakis, N., Lee, J.H.S.: Numerical investigation of the instability for one-dimensional Chapman-Jouguet detonations with chain-branching kinetics. Combustion Theory and Modelling **9**(3), 385–401 (2005). https://doi.org/10.1080/13647830500307758
50. Subbotin, V.A.: Collision of transverse detonation waves in gases. Combustion, Explosion, and Shock Waves **11**(3), 411–414 (1975). https://doi.org/10.1007/BF00740553
51. Grib, S.W., Fugger, C.A., Hsu, P.S., Jiang, N., Roy, S., Schumaker, S.A.: Two-dimensional temperature in a detonation channel using two-color OH planar laser-induced fluorescence thermometry. Combustion and Flame **228**, 259–276 (2021). https://doi.org/10.1016/j.combustflame.2021.02.002
52. Gamezo, V.N., Desbordes, D., Oran, E.S.: Two-dimensional reactive flow dynamics in cellular detonation waves. Shock Waves **9**(1), 11–17 (1999). https://doi.org/10.1007/s001930050134
53. Maxwell, B.M., Bhattacharjee, R.R., Lau-Chapdelaine, S.S.M., Falle, S.A.E.G., Sharpe, G.J., Radulescu, M.I.: Influence of turbulent fluctuations on detonation propagation. Journal of Fluid Mechanics **818**, 646–696 (2017). https://doi.org/10.1017/jfm.2017.145
54. Radulescu, M.I.: A detonation paradox: Why inviscid detonation simulations predict the incorrect trend for the role of instability in gaseous cellular detonations? Combustion and Flame **195**, 151–162 (2018). https://doi.org/10.1016/j.combustflame.2018.05.002
55. Takeshima, N., Ozawa, K., Tsuboi, N., Hayashi, A.K., Morii, Y.: Numerical simulations on propane/oxygen detonation in a narrow channel using a detailed chemical mechanism: formation and detailed structure of irregular cells. Shock Waves **30**, 809–824 (2020). https://doi.org/10.1007/s00193-020-00978-5
56. Vasiliev, A., Gavrilenko, T., Topchian, M.: On the Chapman-Jouguet surface in multi-headed gaseous detonations. Astronautica Acta **17**(4-5), 499–502 (1972)
57. Edwards, D.H., Jones, A.T., Phillips, D.E.: The location of the Chapman-Jouguet surface in a multiheaded detonation wave. Journal of Physics D: Applied Physics **9**(9), 1331–1342 (1976). https://doi.org/10.1088/0022-3727/9/9/010
58. Lee, J.H.S., Radulescu, M.I.: On the hydrodynamic thickness of cellular detonations. Combustion, Explosion and Shock Waves **41**(6), 745–765 (2005). https://doi.org/10.1007/s10573-005-0084-1
59. Kiyanda, C.B., Higgins, A.J.: Photographic investigation into the mechanism of combustion in irregular detonation waves. Shock Waves **23**, 115–130 (2013). https://doi.org/10.1007/s00193-012-0413-8